2013

Solubility extension and phase formation in gas-condensed Co–W nanoclusters

Farhad Golkar
University of Nebraska-Lincoln, farhad518@huskers.unl.edu

Matthew J. Kramer
Ames Laboratory, USDOE, mjkramer@ameslab.gov

Ames Laboratory

Ralph A. Skomski
University of Nebraska-Lincoln, rskomski2@unl.edu

David J. Sellmyer
University of Nebraska-Lincoln, dsellmyer@unl.edu

See next page for additional authors

Published in *Journal of Nanoparticle Research* 15:1638 (April 2013); doi: 10.1007/s11051-013-1638-x

Submitted December 6, 2012; accepted April 4, 2013; published online April 13, 2013.

Solubility extension and phase formation in gas-condensed Co–W nanoclusters

Farhad Golkar[1], M. J. Kramer[2], Y. Zhang[2], R. Skomski[3,4], D. J. Sellmyer[3,4], and J. E. Shield[1,4]

1. Mechanical and Materials Engineering, University of Nebraska, Lincoln, NE 68588, USA
2. Ames Laboratory, Ames, IA 50011, USA
3. Department of Physics & Astronomy, University of Nebraska, Lincoln, NE 68588, USA
4. Nebraska Center for Materials and Nanoscience, University of Nebraska, Lincoln, NE 68588, USA

Corresponding author – Farhad Golkar, email farhad518@huskers.unl.edu

Abstract
Co–W alloy clusters with extended solubility of W in hcp Co were produced by inert-gas condensation. The structural state of the as-deposited Co–W clusters was found to be critically dependent on processing parameters such as the cooling scheme and sputtering power. For the water-cooled clusters, the mean size and percent crystalline were strongly dependent on sputtering power, while the percent crystalline of the liquid nitrogen-cooled clusters was not as affected by the sputtering power. At low sputtering powers, the water-cooled clusters were predominantly amorphous, but became increasingly more crystalline as the sputtering power increased. The predominant crystalline phase was hcp Co(W), but high-resolution transmission electron microscopy revealed that very small and very large clusters contained fcc and Co_3W structures, respectively. For liquid nitrogen cooling the clusters were predominantly amorphous regardless of sputtering power, although at the highest sputtering power a small percentage of the clusters were crystalline. The magnetic properties were dependent on cooling schemes, sputtering power, and temperature, with the highest coercivity of 893 Oe obtained at 10 K for water-cooled clusters sputtered at 150 W. The magnetocrystalline anisotropy of the water-cooled sample increased with increasing sputtering power, with the highest anisotropy of 3.9×10^6 ergs/cm^3 recorded for clusters sputtered at 150 W. For liquid nitrogen-cooled samples, the anisotropy was approximately constant for all sputtering powers.

Keywords: nanomagnetics, cobalt alloys, tungsten alloys, metal clusters, nanofabrication, nanostructured materials, sputter deposition, coercive force, transmission electron microscopy, X-ray diffraction

Introduction

Nanoclusters formed upon condensation from the vapor state are proving to be a rich source of novel, non-equilibrium structures (Jellinek 2008). In particular, the extension of solubility limits, with the potential to significantly alter materials properties, has been predicted in nanoclusters due to finite-size effects (Shirinyan and Gusak 2004; Jesser et al. 1999). Inert-gas condensation (IGC) is a non-equilibrium processing route to produce nanoparticles, making it an ideal technique to explore new materials and structures (Koshkin and Slezov 2004; Mukherjee et al. 2012). In IGC, the cluster structure depends on processing conditions, notably the sputtering power when dc magnetron sputtering is used to create the gas phase (Balasubramanian et al. 2011; Patterson et al. 2010; Qiu and Wang 2006), and the temperature inside the cluster-forming chamber (Golkar et al. 2012). Further, the structural state in clusters is size-dependent, especially in Co nanoclusters, where the fcc structure was predominant in sub-6 nm clusters, with the volume fraction of the hcp structure increasing with increasing cluster size (Yamamuro et al. 1999).

In permanent magnetism, current research has recently shifted focus to rare earth-free permanent magnet alloys as a consequence of increased worldwide demand on rare earth elements (Kramer 2010). The significant challenge is to develop materials with sufficient anisotropy to induce large coercivity values without the RE elements. The ideal materials require a high proportion of ferromagnetic elements such as Fe or Co. Recent theoretical work has shown that solid solutions of 5d transition metals in Co or Fe crystalline compounds induce an increase in magnetocrystalline anisotropy (Skomski et al. 2010; Kashyap et al. 2011), thus potential candidates for permanent magnet alloys. Because of their larger size, there is limited solubility of heavy transition metals, such as W, in the 3d elements, particularly Fe and Co. The equilibrium solubility limit of W in hcp Co is approximately 0.5 at.% up to 750°C (Nagender Naidu et al. 1992). In this study, inert-gas condensation has been used to synthesize non-equilibrium Co–W clusters and to study their formation, structure, and magnetic properties. The focus is to dissolve W into hcp Co to determine if an increase in magnetocrystalline anisotropy is observed.

Experiments

Co–W alloy clusters were produced by inert-gas condensation (Haberland et al. 1992). DC magnetron sputtering was used to form the atomic gas from a Co–W composite target. The base pressure of the system was less than 10^{-7} Torr. An Ar/He gas mixture was introduced into the cluster-forming chamber, in which Ar was used for the sputtering and He was used to ensure temperature uniformity inside the chamber. Deposition rates were measured in situ using a quartz crystal thickness monitor. Clusters were produced using sputtering powers of 50, 100, and 150 W, while the nucleation chamber was cooled by either water or liquid N_2.

The cluster-forming chamber was cooled either by flowing water or liquid nitrogen to maintain a temperature of approximately 18 or –120°C, respectively. The composition of the Co–W nanoclusters was set using W plugs inset in a Co target. For this study, W plugs comprising approximately 16% of the ''racetrack'' typical of magnetron sputtering was employed, which according to typical sputtering yields (Chapman 1980) would result in a composition of approximately 92 at.% Co and 8 at.% W. For magnetic measurements, the Co–W clusters were imbedded in a C matrix by alternate deposition from the cluster source and an RF source positioned perpendicular to the cluster source. Overall thickness of the composite films, which were deposited on a Si substrate, was approximately 30 nm. The magnetic measurements were conducted at 10 and 300 K using a quantum design magnetic property measurement system SQUID magnetometer with a maximum field of 7 T. The sample signal was determined by subtracting the contributions from the Si substrate and the C matrix.

For characterization using transmission electron microscopy (TEM), the Co–W clusters were deposited directly onto graphite support films, and to prevent oxidation a thin layer of C was deposited after cluster deposition. TEM was accomplished using a JEOL 2010 operating at 200 kV and a FEI Tecnai G^2 F20 operating at 200 kV. The compositions of the clusters were determined by energy-dispersive X-ray spectroscopy (EDS) operating in the scanning TEM (STEM) mode in the FEI Tecnai. Area scans encompassing a number of clusters were used to obtain an average composition. Image analysis was accomplished by ImageJ. For phase characterization the Rigaku Multiflex X-ray diffractometer with Cu Kα radiation was used. Cluster films approximately 30 nm thick were deposited for X-ray diffraction (XRD) studies.

Results and discussion

Water cooling

TEM images of the as-deposited water-cooled clusters at sputtering powers of 50, 100, and 150 W are presented in figure 1. The clusters are in the sub-10 nm range. It was found that the average size of the clusters increased with increasing sputtering power (inset fig. 1). The sizes were estimated to be 5.7 ± 1.8, 6.6 ± 2.1, and 7.1 ± 2.8 nm for the sputtering powers 50, 100, and 150 W, respectively. EDS analysis of both individual clusters and area scans of the clusters showed that the composition was consistent for all sputtering powers, and was approximately 95 at.% Co and 5 at.% W. This composition lies in the two-phase region of Co_3W + hcp Co in the phase diagram (Nagender Naidu et al. 1992).

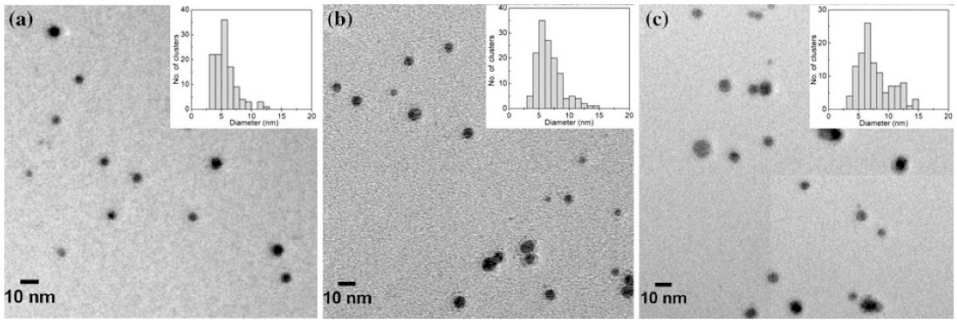

Figure 1. TEM images and (*inset*) cluster size histogram of the as-deposited water-cooled Co–W clusters produced with magnetron sputter power of (a) 50 W, (b) 100 W, and (c) 150 W.

The XRD patterns of the water-cooled as-deposited clusters for all sputtering powers are shown in figure 2. The standard diffraction peaks corresponding to hcp Co and $Co_3W$are indicated as dotted and dashed lines, respectively. At low sputtering power [curve (a) in fig. 2] the XRD results indicate that the clusters have an amorphous structure, characterized by a broad diffraction maximum at 2θ~44°. As the sputtering power increases the XRD patterns reveal that a number of broad peaks start to appear. The broad peaks are due to the size of the diffracting regions. The good agreement with hcp Co peak locations indicates the presence of crystalline hcp Co in the material. However, because of structural similarities between hcp Co and Co_3W (Villars 1997), some diffractions lines are nearly coincident. The most definitive peaks indicating the Co_3Wstructure occur at 2θ~29.6 and 46.5°. No peaks were observed at these locations, suggesting that the predominant structure is hcp Co. Additionally, no diffraction peaks were observed that corresponded to the (111) and (200) planes of fcc Co structure; thus, the diffraction peaks clearly index to the hcp Co structure. The peak observed at 2θ~29° for the sample sputtered at 150 W [curve (c) in fig. 2] is an instrumental artifact.

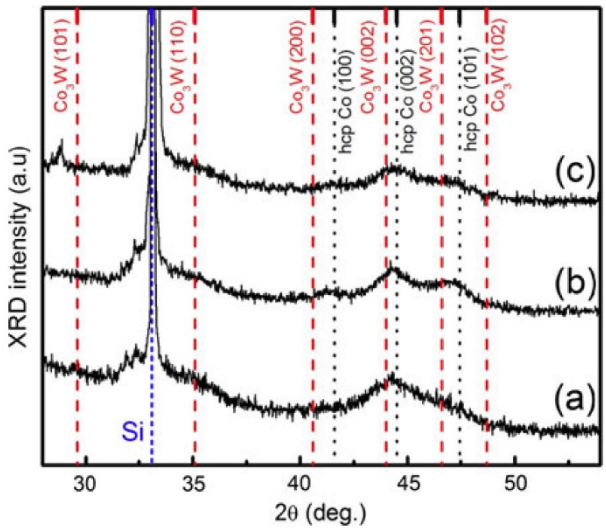

Figure 2. X-ray diffraction pattern of the as-deposited water-cooled samples produced at (a) 50 W, (b) 100 W, and (c) 150 W. Dashed and dotted lines show the standard diffraction lines for Co_3W and hcp Co structure, respectively.

High-resolution TEM (HRTEM) images of the as-deposited water-cooled clusters confirmed that the clusters have a predominantly amorphous structure at low sputtering power (fig. 3a), although some lattice fringes were observed. The selected-area electron diffraction (SAD) pattern also revealed a predominantly amorphous structure at low sputtering power, indicated by diffuse rings, while the small number of crystalline particles is indicated by the few discrete diffraction spots. The plane spacings determined from these diffraction spots and measured from the lattice fringes were consistent with the hcp Co structure. With increasing sputtering power the lattice fringes became more prevalent, indicating a larger number of crystalline particles (fig. 3b, c). In clusters oriented such that lattice fringes are observed, they tend to extend across the entirety of the cluster, indicating that the clusters are single-crystalline. The SAD pattern of the 150 W sample (fig. 3d) was indexed to a hcp Co structure with lattice parameters a ~ 0.262 nm and c ~ 0.408 nm, close to literature values (Villars 1997).

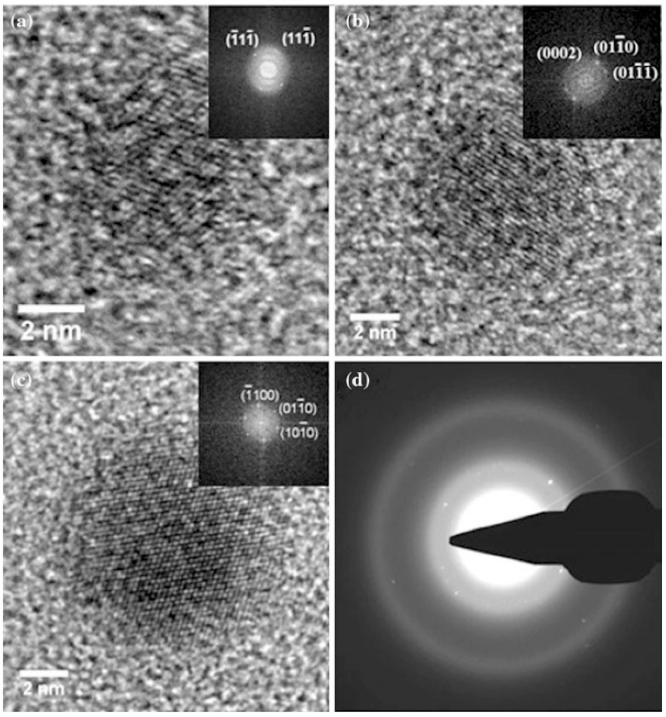

Figure 3. High-resolution TEM image of the individual as-deposited water-cooled Co–W clusters produced at (a) 50 W, (b) 100 W, and (c) 150 W. *Inset* FFT of the HRTEM image where the diffraction spots correspond to the (a) [011] zone axis of fcc structure, (b) [$2\bar{1}\bar{1}0$] zone axis of the hcp structure, and (c) [0001] zone axis of the hcp structure. (d) SAD pattern of the as-deposited water-cooled 150 W sample.

The structures of the clusters can also be determined from high-resolution TEM images using fast-Fourier transforms (FFT). Clusters close to the mean size (~7 nm) were determined to have the hcp Co structure (fig. 3b). However, an fcc structure was observed in smaller clusters (< 5 nm) as, for example, shown by the [011]-indexed FFT of figure 3a. The lack of fcc signatures in both XRD and SAD patterns would indicate that there is a relatively low volume fraction of the smaller clusters (see, for example, the histogram of fig. 1). The appearance of the fcc structure in smaller clusters and the hcp structure in larger clusters is consistent with earlier work in pure Co nanoparticles by Yakamora et al. (1999).

While larger (> 12 nm) clusters indicated single-crystalline hcp structures in high-resolution images (fig. 4a), high-angle annular dark field (HAADF) STEM images clearly show unique compositional variations within clusters, with brighter regions indicating a higher average atomic number (fig. 4). EDS analysis confirmed that the brighter regions are enriched in W. It was also noted that these larger clusters are distinctly faceted. The ''wagon wheel'' contrast in the STEM HAADF images suggests two-phase formation in these clusters. The similarity in structure between hcp Co and Co_3W allows distinct segregation patterns while maintaining crystallographic relationships between the two phases. In hcp Co the stacking of close-packed planes are ABAB (fig. 4c, left). The Co_3W consists

of an ordered substitution of two W atoms in a hcp Co supercell of 8 atoms, as can be seen in figure 4c (right), with each W atom replacing one Co atom on each layer. This gives lattice parameter relationships between hcp Co and Co_3W of

$$^{a}Co_3W \approx 2a_{hcp\ Co}$$

$$^{c}Co_3W \approx c_{hcp\ Co}$$

A model structure of the larger, faceted clusters is shown in figure 4d. This proposed structure has an ordered substitution of W in hcp Co along the [10$\underline{1}$0] directions and is consistent with both HRTEM and HAADF images. The formation of the two equilibrium phases in the larger clusters indicates an approach to equilibrium phase relationships as the cluster size increases, with the transition occurring in this system at ~10 nm. At smaller cluster sizes, the cluster's inability to support multiple phases leads to a supersaturated solid solution of W in hcp Co.

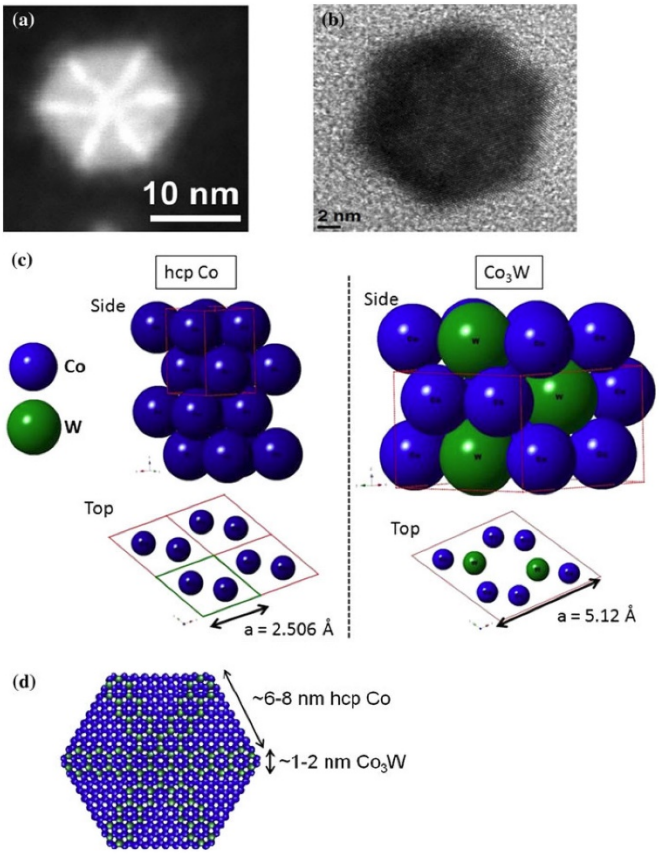

Figure 4. (a) High-angle annular dark field (HAADF) STEM image of the Co–W cluster showing compositional variations within the cluster. (b) High-resolution TEM of the faceted cluster. (c) Structural model of hcp Co and Co_3W (*blue spheres* represent Co atoms and *green spheres* represent W atoms) are from *side* and *top* view. (d) Proposed structure of the ''wagon wheel'' (seen from the *top*).

The magnetic properties of the as-deposited water-cooled Co–W clusters measured at 10 and 300 K are presented in table 1. The hysteresis curves normalized to the largest measured magnetization for the different sputtering powers and temperatures are presented in figure 5. At 300 K, the coercivity and remanence ratio increased slightly with increasing sputtering power. The low coercivity is a result of the predominantly amorphous structure in the clusters. At 10 K, both coercivity and remanence ratio increased with increasing sputtering power, with the highest coercivity of 893 Oe for the 150 W sample. The value of the magnetocrystalline anisotropy K_1 was found by the law of approach to saturation (Kneller 1962; Hadjipanayis et al. 1981). In this technique, the high-field magnetization measurements are least-squared fitted to the equations

$$M = M_s\left(1 - \frac{A}{H^2}\right) + \chi H \tag{1}$$

where χ is the high-field susceptibility and A is a constant that includes the anisotropy constant K_1 according to the relationship

$$A = \frac{4}{15}\frac{K_1^2}{M_s^2} \tag{2}$$

The increase of coercivity, remanence ratio, and magnetocrystalline anisotropy is due to the increase in the percent crystallinity of the hcp Co which occurs with increasing sputtering power. However, the observed coercivities are lower than what is typical for hcp Co, and the highest magnetocrystalline anisotropy observed here, 3.9×10^6 ergs/cm^3, is slightly lower than that of bulk hcp Co [$K_1 \sim 4.5 \times 10^6$ ergs/cm^3 (Cullity and Graham 2009)]. Typically, the magnetic anisotropy of hard-magnetic materials tends to be lower in nanoclusters due to the high fraction of surface atoms (Balasubramanian et al. 2011; Akdogan et al. 2011). Here it appears that any enhancement in K_1 due to W additions is more than offset by the surface effects. Additionally, the saturation magnetizations were significantly reduced as compared to pure hcp Co (1,422 emu/cm^3). The saturation magnetization also appears to decrease as the crystallinity increases, suggesting that atomic ordering of the W suppresses the magnetic moment of Co. Note that the largest particles had an obvious two-phase mixture of hcp Co and Co_3W. Since Co_3W has a low magnetization, it is possible that slightly smaller clusters may have local (short-range) ordering of the W which acts to suppress the magnetization as it does in Co_3W. The decrease in magnetization is also consistent with theoretical calculations of W-doped Co (Kashyap et al. 2011). As the particles get larger the energy penalty for forming the coherent interfaces is likely small compared to the formation enthalpy of a hyper-stoichiometric hcp Co with W. Further work is necessary to clarify this effect.

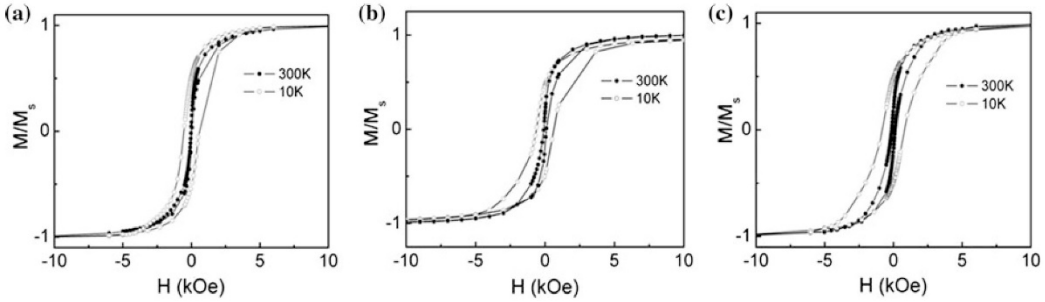

Figure 5. Hysteresis curves normalized with the largest measured magnetization for the as-deposited water-cooled Co–W clusters by using power setting. (a) 50 W, (b) 100 W, and (c) 150 W

Table 1. Magnetic properties of the as-deposited water-cooled Co–W clusters measured at 10 and 300 K

Sample (W)	Coercivity (Oe)		Saturation magnetization, M_s (emu/cm^3)		M_r/M_s		K_1 (×10^6 ergs/cm^3)	
	300 K	10 K	300 K	10 K	300 K	10 K	300 K	10 K
50	24	537	822	860	0.06	0.44	2.1	1.9
100	95	623	472	565	0.18	0.47	2.7	3.2
150	150	893	380	452	0.20	0.48	2.1	3.9

Liquid nitrogen cooling

TEM images of the as-deposited liquid nitrogen-cooled clusters are shown in figure 6. The sizes of the clusters were estimated to be 6.3 ± 3.7, 4.4 ± 2.0, and 4.9 ± 2.5 nm for the sputtering powers 50, 100, and 150 W, respectively. The smaller mean size of these clusters compared to the water-cooled clusters is believed to be due to the lower temperature during the nucleation process. The lower temperature decreases the critical nucleus size and suppresses subsequent growth of clusters.

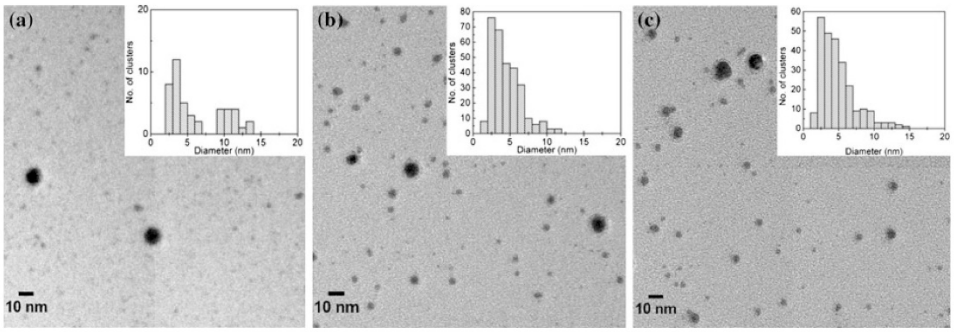

Figure 6. TEM image of the as-deposited liquid nitrogen-cooled Co–W clusters produced at sputtering power. (a) 50 W, (b) 100 W, and (c) 150 W

XRD patterns (fig. 7) of the as-deposited samples revealed only a broad diffraction maximum at $2\theta \sim 44°$ for clusters produced using a power setting of 50 W. The broad peak suggests an amorphous structure. No additional peaks appeared in the pattern even with increasing sputtering power. This indicates that the samples remained amorphous regardless of sputtering power. Note that the peak observed at $2\theta \sim 36°$ for sample sputtered at 50 W [curve (a) in fig. 7] is an instrumental artifact.

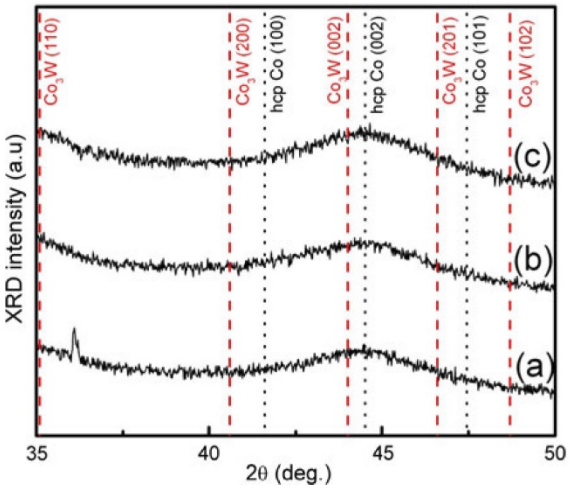

Figure 7. X-ray diffraction pattern of the as-deposited liquid nitrogen-cooled samples produced at (a) 50 W, (b) 100 W, and (c) 150 W. *Dashed* and *dotted lines* show the standard diffraction lines for Co_3W and hcp Co, respectively.

HRTEM and SAD images of the as-deposited liquid nitrogen-cooled clusters produced using power settings of 50 and 100 W indicated that the clusters were amorphous. Neither diffraction spots nor lattice fringes were visible in the images at these powers. However, clusters produced with a power setting of 150 W displayed some lattice fringes in the HRTEM images and also discrete diffraction spots in the SAD pattern (fig. 8), indicating that some particles are crystalline at this power. The FFT of the cluster shown in figure 8 (inset fig. 8) was indexed to the [$2\underline{11}0$] zone axis of the hcp structure. Indexing of the few reflections observed in the SAD pattern was consistent with a hcp structure with lattice parameters $a \sim 0.243$ nm and $c \sim 0.416$ nm, consistent with the FFT.

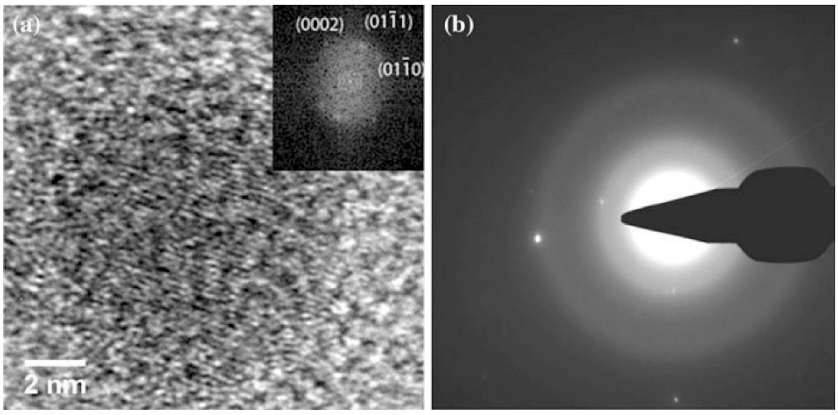

Figure 8. (a) HRTEM image of the individual as-deposited liquid nitrogen-cooled Co–W cluster produced at 150 W. *Inset* FFT of the HRTEM image shows the diffraction spots corresponding to the [2$\bar{1}\bar{1}$0] zone axis of hcp structure. (b) SAD pattern of 150 W samples

At 300 K, the as-deposited liquid nitrogen-cooled sample sputtered at 50 W showed superparamagnetic behavior, with both coercivity and remanence ratio being zero, while some hysteresis was observed for samples processed at 100 and 150 W (fig. 9; table 2). The hysteretic behavior for the latter two samples may be due to the (small) increase in cluster size, but more likely due to the increase in structural order, which would increase the anisotropy, and consequently the blocking temperature. At 10 K, the 50 W sample showed ferromagnetic behavior, with H_c ~ 423 Oe and M_r/M_s of 0.45. The coercivity also increased for the 100 and 150 W samples. The magnetocrystalline anisotropy values obtained for the as-deposited liquid nitrogen-cooled samples were approximately constant for all sputtering powers (K_1 ~ 0.5 × 10^6 ergs/cm^3). The values were well below the values obtained for water-cooled samples which are due to the lower degree of crystalline particles observed in the liquid nitrogen-cooled samples.

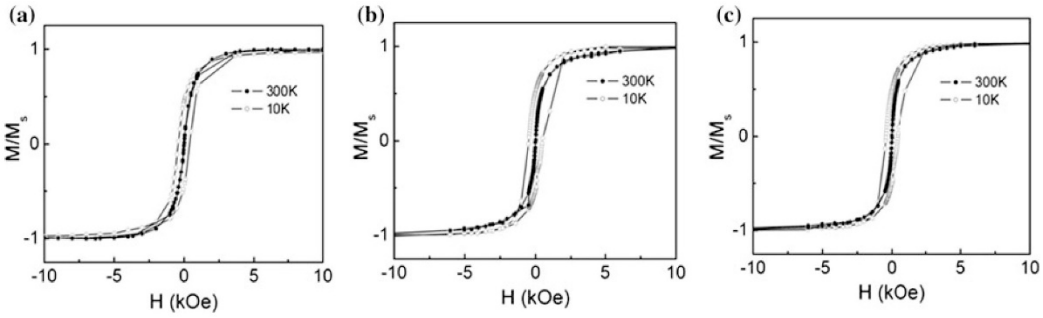

Figure 9. Hysteresis curves normalized with the largest measured magnetization for the as-deposited liquid nitrogen-cooled Co–W clusters using power setting. (a) 50 W, (b) 100 W, and (c) 150 W

Table 2. Magnetic properties of the as-deposited liquid nitrogen-cooled Co–W clusters measured at 10 and 300 K

Sample (W)	Coercivity (Oe)		Saturation magnetization, M_s (emu/cm^3)		M_r/M_s		K_1 (×10^6 ergs/cm^3)	
	300 K	10 K	300 K	10 K	300 K	10 K	300 K	10 K
50	0	423	358	409	0	0.45	1.1	1.2
100	11	481	293	463	0.03	0.45	2.2	2.0
150	14	470	345	485	0.04	0.45	1.1	1.0

The coercivity as a function of sputtering power for both cooling schemes is shown in figure 10. The liquid nitrogen-cooled values were still lower than for water-cooled samples regardless of the sputtering power, which is due to the increased percent crystalline in water-cooled samples compared to liquid nitrogen-cooled samples.

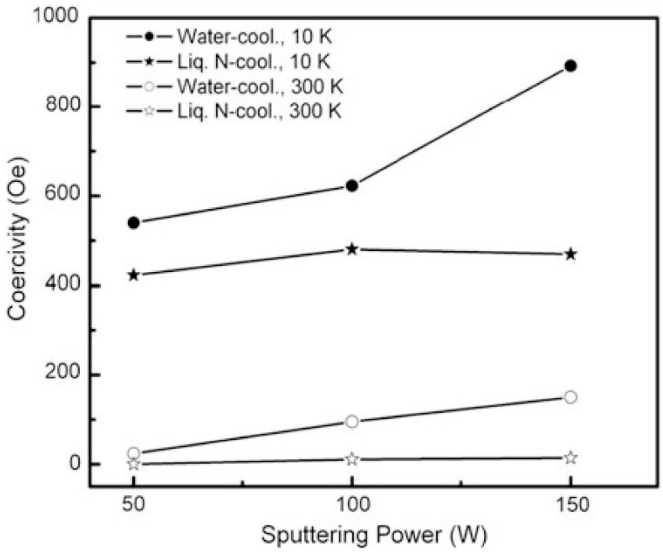

Figure 10. Coercivity for both water- and liquid nitrogen-cooled samples as a function of sputtering power.

Conclusion

Sub-10 nm Co–W alloy clusters were deposited by IGC method. The structure and formation of the as-deposited clusters were controlled by different cooling schemes and sputtering powers. EDS analysis of both individual clusters and area scans revealed consistently that the composition of the clusters was approximately 95 at.% Co and 5 at.% W regardless of processing conditions, which is approximately 5 atomic percent above the equilibrium solubility limit of W in hcp Co. For the water-cooled samples, XRD and transmission electron microscopy revealed that at low sputtering power the structures formed were predominantly amorphous, while for high sputtering power crystalline hcp Co clusters with W in solid solution were formed. Hexagonal shaped clusters were observed at

the highest sputtering power for the as-deposited water-cooled samples. HAADF/STEM images showed compositional variations within the clusters, with the brighter regions being more W rich. For the liquid nitrogen-cooled samples, TEM images and XRD showed that the samples were amorphous for power settings 50 and 100 W while for the 150 W diffuse rings together with discrete diffraction spots were observed in the SAD images. The magnetic measurements showed that the coercivity and remanence ratio of the water-cooled clusters were higher than that for liquid nitrogen-cooled samples for all sputtering powers and temperatures. The crystalline clusters of water-cooled samples were determined to have higher coercivity at both 10 and 300 K. The highest coercivity of 893 Oe was obtained for 150 W sample at 10 K, and the magnetocrystalline anisotropy corresponding to this sputtering power was estimated to be 3.9×10^6 ergs/cm^3, which is slightly lower than that for bulk hcp Co.

Acknowledgments – This work was supported by the Department of Energy-Energy Efficiency and Renewable Energy, Vehicles Technology Office, PEEM program, under Contract No. DE-AC02-07CH11358 for the operation of Ames Laboratory (USDOE) and sub-contract no. SC-10-343 to the University of Nebraska–Lincoln.

References

Akdogan O, Li W, Hadjipanayis GC, Sellmyer DJ (2011) Synthesis of single-crystal Sm–Co nanoparticles by cluster beam deposition. *J Nanopart Res* 13:7005–7012.

Balasubramanian B, Skomski R, Li X, Valloppilly S, Shield JE, Hadjipanayis GC et al (2011) Cluster synthesis and direct ordering of rare-earth transition-metal nanomagnets. *Nano Lett* 11:1747–1752.

Chapman B (1980) *Glow discharge processes: sputtering and plasma etching*. Wiley, New York.

Cullity BD, Graham CD (2009) *Introduction to magnetic materials*, 2nd edn. Wiley, Hoboken.

Golkar F, Kramer MJ, Zhang Y, McCallum RW, Skomski R, Sellmyer DJ et al (2012) Structure and magnetic properties of Co–W clusters produced by inert gas condensation. *J Appl Phys* 111:07B524.

Haberland H, Karrais M, Mall M, Thurner Y (1992) Thin films from energetic cluster impact: a feasibility study. *J Vac Sci Technol A* 10(5):3266–3271.

Hadjipanayis GC, Sellmyer DJ, Brandt B (1981) Rare-earth-rich metallic glasses. I. Magnetic hysteresis. *Phys Rev B* 23(7):3349–3354.

Jellinek J (2008) Nanoalloys: tuning properties and characteristics through size and composition. *Faraday Discuss* 138:11–35.

Jesser WA, Shiflet GJ, Allen GL, Crawford JL (1999) Equilibrium phase diagrams of isolated nanophases. *Mater Res Innov* 2:211–216.

Kashyap A, Manchanda P, Sahota P, Skomski R, Shield J, Sellmyer D (2011) Anisotropy of W in Fe and Co. *IEEE Trans Magn* 47(10):3336–3339.

Kneller E (1962) *Ferromagnetisms*. Springer, Berlin.

Koshkin VM, Slezov VV (2004) Doping nanoparticles. *Tech Phys Lett* 30(5):367–369.

Kramer D (2010) Concern grows over China's dominance of rare-earth metals. *Phys Today* 63(5):22–24.

Mukherjee P, Zhang Y, Kramer MJ, Lewis LH, Shield JE (2012) L10 structure formation in slow-cooled Fe–Au nanoclusters. *Appl Phys Lett* 100:211911.

Nagender Naidu SV, Sriramamurthy AM, Rama Rao P (1992) In: Okamoto H, Subramanian PR, Kacprzak L (eds) *Binary alloy phase diagrams*, vol 2. ASM International, Materials Park, p 1257.

Patterson MM, Cochran A, Ferina J, Litwinowics VJ, Rui X, Zimmerman TA et al (2010) Early stages of direct L10 FePt nanocluster formation: the effects of plasma characteristics. *J Vac Sci Technol B* 28:273.

Qiu JM, Wang JP (2006) Monodispersed and highly ordered L10 FePt nanoparticles prepared in the gas phase. *Appl Phys Lett* 88:192505.

Shirinyan AS, Gusak AM (2004) Phase diagrams of decomposing nanoalloys. *Phil Mag* 84(6):579–593.

Skomski R, Sharma V, Balamurugan B, Shield JE, Kashyap A, Sellmyer DJ (2010) Anisotropy of doped transition—metal magnets. In: Kobe S, McGuiness P (eds) *Proc. REPM'10*. Jozef Stefan Institute, Ljubljana, pp 55–60.

Villars P (1997) *Pearson's handbook of crystallographic data for intermetallic phases*, Desk edn. ASM International, OH.

Yamamuro S, Sumiyama K, Konno TJ, Suzuki K (1999) Structural and magnetic evolution in self-assembling process of nanometer-sized co clusters. *Mater Trans JIM* 40(12):1450–1455.